International Journal of Modern Physics B, Vol. 15, No. 17 (2001) 2301–2333

A UNION OF THE REAL-SPACE AND RECIPROCAL-SPACE VIEW OF THE GaAs(001) SURFACE

V. P. LaBELLA, Z. DING, D. W. BULLOCK,
C. EMERY and P. M. THIBADO

Department of Physics, The University of Arkansas,
Fayetteville, Arkansas 72701

Received 12 April 2001

A union of the real-space and reciprocal space view of the GaAs(001) surface is presented. An optical transmission temperature measurement system allowed fast and accurate temperature determinations of the GaAs(001) substrate. The atomic features of the GaAs(001)-(2×4) reconstructed surface are resolved with scanning tunneling microscopy and first principles density functional theory. In addition, the 2D lattice-gas Ising model within the grand canonical ensemble can be applied to this surface to understand the thermodynamics. An algorithm for using electron diffraction on the GaAs(001) surface to determine the substrate temperature and tune the nanoscale surface roughness is presented.

1. Introduction

The (001)-oriented surface of GaAs is one of the most technologically important surfaces in the family of zinc-blende III–V, or compound semiconductors. This is primarily due to the numerous optoelectronic devices and high-speed transistors, which are fabricated from these materials. The ability to fabricate single-crystal device structures composed of only a few atomic layers of different materials sandwiched between one another with atomically abrupt transitions is part of what makes III–V materials attractive for devices such as solid-state lasers and diodes. However, unlike silicon based devices, these layered heterostructures must be grown using epitaxial methods, where layers of atoms are deposited on an atomically clean surface under ultra-high vacuum (UHV) conditions. Essentially, epitaxy is a surface driven phenomenon and a better understanding of the fundamental physics behind surfaces and adatom-surface interactions can lead to a better understanding of growth. Specifically, for providing approaches and input parameters for predictable models for device fabrication. In addition, this understanding is important for novel nanoscale devices where the interfaces constitute a significant fraction of the entire device structure.

While numerous studies of the GaAs(001) surface abound,[1–23] including several review articles,[24,25] some recent studies and advances in instrumentation have

provided new insight into this important surface.[26–29] These discoveries, spurred by both *in situ* scanning tunneling microscopy (STM) and accurate (±2°C) temperature control of the substrate, center mainly around two areas. First, resolving the atomic structure of the GaAs(001)-(2 × 4)-reconstructed surface using bias-dependent STM and first-principles density functional calculations.[28] Secondly, understanding the complex thermodynamic relationship between the surface morphology, substrate temperature, and arsenic beam equivalent pressure (BEP).[29] This paper will review these recent advances in instrumentation and its role in understanding the GaAs(001) surface. In doing so, a union in the real-space view of the surface as seen with STM and the reciprocal space view of the surface as seen with electron diffraction will be presented.

2. Accurate Temperature Control of the GaAs Substrate

2.1. *Difficulties in determining the substrate temperature within an MBE system*

As traditionally practiced, MBE suffers from poor day-to-day repeatability, which is due, in part, to the lack of any means to accurately sense and control one basic process parameter: namely, the substrate temperature. This problem arises because the typical sensor used for temperature control is a thermocouple, which cannot be in good thermal contact with the substrate if one wants to produce high-quality, high-uniformity material. The inaccuracies in substrate temperature, in turn, affect the overall progress within the MBE community at large. The reason for this is that the temperature-time profile used to produce a high-quality growth at one institution cannot be transferred to other institutions. The MBE community has tried to minimize these difficulties through the implementation of optical pyrometers for substrate temperature determination. Unfortunately, the accuracy of pyrometers is limited by stray light from the source ovens and substrate heater filaments. In addition, pyrometer readings are affected by films deposited on the pyrometer viewport and by lack of knowledge of sample emissivity (which in many cases is changing during the growth of the structure). Finally, if one uses direct radiative heating of the substrate the pyrometer becomes flooded with the infrared radiation of the heater filaments, making the technique even less accurate.[30]

Other workers have suggested the use of fundamental optical properties, such as the band gap of a semiconductor and its temperature dependence, as a vehicle for obtaining accurate and reproducible substrate temperatures.[30] One implementation of this idea is realized by using the broadband light emitted from the substrate heater filaments as the light source for performing an optical transmission measurement on the substrate.[30,31] Using the substrate heater as a light source is very clever and has many advantages over thermocouple sensors and pyrometers. Namely, it determines the temperature without requiring physical contact with the substrate and this approach is not affected by films being deposited on the pyrometer viewport.[31] In addition, this approach does not require internal modifications

to the MBE machine to implement. However, there are two disadvantages with this approach. First, the signal to noise ratio is affected by stray light, since the intensity of the heater light cannot be modulated. Second, the light source is not available to measure the substrate temperature when the heater power is turned off. Another implementation of *in situ* band gap determination, is to bring white light in the pyrometer port and measure the band-edge reflection spectroscopy using the back-reflected light coming out of the pyrometer viewport.[32] This method works well for bare substrates but suffers from optical interference effects, especially when the films are smooth and uniform in thickness (precisely what one wants to achieve with MBE).

The most successful non-contact temperature measurement scheme was achieved by installing an optical pipe inside the MBE machine that allows an alternate light source to be brought to the back side of the substrate. This has been successfully implemented in MBE machines that have an in-line optical path to the backside of the substrate.[33] Supplying an alternate light source which can be chopped prior to entering the substrate has proven to be the most precise substrate temperature measurement method available.[34] However, in MBE machines where the sample is mounted on a manipulator that rotates about a perpendicular flange axis (such as the Riber 32), implementing this technique is a bit more difficult, although not impossible. Here, a simple and robust solution has been used for integrating a non-contact transmission thermometry sample temperature measurement scheme into a Riber 32 MBE machine.[26] The Riber 32 MBE machine falls into a class of MBE machines which utilizes a rotating manipulator for sample transfers, which makes this integration unusually complicated. The fundamental band gap of the substrate is measured from the transmission spectrum obtained after passing white light through the substrate. This approach allows the substrate temperature to be measured over a wide-temperature range (e.g., 0–700°C for GaAs) without making physical contact to the substrate. The temperature of the substrate is known within ±2°C and is updated approximately every second.

2.2. *Implementation of the band-gap temperature measurement system*

There are primarily two custom components that made the incorporation of the optical thermometry system possible. First, a shaped quartz rod that guides the light from a fiber bundle to the back side of the substrate (see Fig. 1). The quartz rod has a diameter of 2 mm and the ends are flame polished to be optically flat. One end of the quartz rod is positioned 1–2 mm away from the substrate. Due to the high temperature stability properties of quartz, there are no contamination issues to consider (even though the quartz rests only millimeters away from the hot sample and heater filaments). If a stainless steel coated fiber pipe was used this close to the heater, severe outgasing and subsequent contamination problems would occur. The quartz rod has a 90° bend with a radius of curvature of 25.4 mm

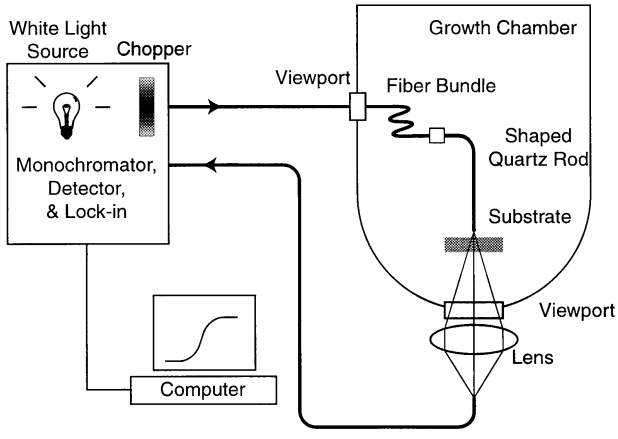

Fig. 1. Schematic diagram showing the entire optical delivery system used for transmission thermometry measurements. The system uses a 20 W white light source which is passed through a chopper. The light then moves through a fiber bundle to a viewport on the ultra-high vacuum (UHV) growth chamber. Inside the vacuum chamber the light travels through a fiber bundle, and then through the shaped quartz rod to the back side of the substrate. The transmitted light is collected through another viewport on the front side of the substrate, and is then fed into the monochromator. After using lock-in detection, a computer digitizes the transmission spectra, and calculates the substrate temperature.

and an overall length of 200 mm, so that the other end of the rod directly faces the conflat flange holding the sample manipulator. The second critical component which made the integration successful is an ultra-high vacuum (UHV) compatible optical fiber bundle, which is attached to one end of the quartz rod and directs the light to an optical fiber port on the manipulator flange. The individual fibers are made of borosilicate and are not coated. The fiber bundle is encased in a stainless steel monocoil, and between the fiber bundle and the stainless steel is a layer of a fiberglass material called "Natural Silverflex". This material is used to avoid fiber breakage and is UHV compatible, unlike the conventional polymer materials used to coat fibers (the fiber bundle was supplied by Fiberguide Industries). The fiber–fiber feed through is simply a standard glass viewport with a special mount which rigidly supports the fiber flat against the viewport (the fiber–fiber UHV conflat feed through was supplied by CI Systems). The sample and the quartz rod assembly rotate as a rigid body 180° between the sample introduction position and the sample growth position about a line perpendicular to the manipulator flange and approximately centered on the manipulator flange. A 60 cm long fiber bundle connects the quartz rod to the manipulator flange which are separated by about 20 cm. The extra 40 cm of fiber length allows the optical system to easily accommodate the 180° twist without breaking. In addition, the fiber bundle is mounted approximately 10 cm away from the center of the manipulator flange and thus only needs to flex ±5° during the ±90° swing of the sample from transfer to growth position. The quartz rod is only fixed at the point where it attaches to

the fiber bundle, otherwise it simply rests against the manipulator components, providing a strain free mount that allows for independent thermal expansion and contraction. The entire assembly is UHV capable, and our system reaches a base pressure of 3×10^{-11} Torr when cooled with liquid nitrogen.

The quartz rod and fiber bundle assembly are the only components inside the vacuum chamber. On our manipulator, the optical delivery components are relatively simple to install and replace. The MBE machine is a custom modified commercial system. The primary internal modifications were moving the thermocouple sensor from the center of the 3-in. heater to a new position approximately 5 mm away, and also making a 3 mm diameter hole through a polycrystalline boron nitride (PBN) plate that sits between the heater filaments and the substrate. As stated above, the quartz rod simply rests against the edge of the PBN plate and is only held to a rigid mount at the other end. This allows the quartz rod and manipulator assemble to flex without putting tension on one another. Our entire chamber has been cycled from room temperature to 200–250°C several times without any damage occurring to the quartz rod or the fiber bundle. In addition, the manipulator is rotated from the sample transfer position to the sample growth position several times per day, and this motion has never caused the quartz rod or fiber bundle to fail. In order to upgrade an existing MBE system to utilize the optical delivery system described here, one key requirement is having a pyrometer viewport in front of the sample while in the growth position (ideally, directly in front of the sample). A second requirement is to modify the sample heater and manipulator to make space for the quartz rod and fiber bundle.

Outside the vacuum chamber we used commercially available hardware and software (model NTM1 from CI Systems, Israel) system for performing the optical transmission measurements, shown schematically in Fig. 1. This system uses chopped white light from a 20 W lamp in order to separate our light source from stray light due to the heater, ion gauges, and cells. This light is directed to the back side of the substrate using the fiber bundle and shaped quartz rod discussed earlier. The light which is transmitted through the wafer is collected through a viewport on the growth surface side of the sample. Note, the optical throughput of the interface components is less than 2.5%. The primary loss of light collection is due to beam divergence from the quartz rod to the viewport. A simple lens system collects the light and focuses it onto a fiber bundle, after which the light is piped into a fast-scan grating monochromator with a silicon-germanium detector and a lock-in amplifier. A computer reads the transmission spectra and then calculates the fundamental band gap using either a first or second derivative technique. The temperature of the substrate is determined by comparing the band gap obtained from the above measurement with one obtained from a database. The entire process of collecting and digitizing the light intensities over a wavelength range from 600 to 1600 nm and extracting a temperature is about once per second. We now use the substrate temperature obtained with this system as a feedback for setting the amount of current delivered to the heater filaments.

2.3. *Sources of errors in traditional temperature measurement systems*

To demonstrate performance of the system, several experiments were performed using an "EpiReady" semi-insulating GaAs(001) 2-in. wafer that was loaded into the MBE system without any chemical cleaning. The oxide was removed and $\sim$ 1-μm-thick GaAs buffer layer was grown using a Ga to As_4 beam equivalent pressure (BEP) ratio of 15, a substrate temperature of 580°C, and a growth rate of 1 μm/h as determined by reflection high-energy electron diffraction (RHEED) oscillations.

Transmission spectra as a function of photon energy were acquired, by cooling the sample to room temperature and then subsequently heating it to 100°C using a constant current power supply. The current was manually adjusted until the temperature was 100 $\pm$ 2°C and did not change for 30 minutes. At the end of this period, a transmission spectrum was recorded. This procedure was repeated for 100°C increments up to 600°C. The transmission spectra obtained from this experiment are shown in Fig. 2. The sharp drop in the transmission curves is due to a sharp increase in the absorption of light due to band-to-band transitions. The fundamental band gap decreases in an approximately linear manner as the temperature is increased from 0 to 700°C.

The advantage of supplying light to the back of the substrate is that once the

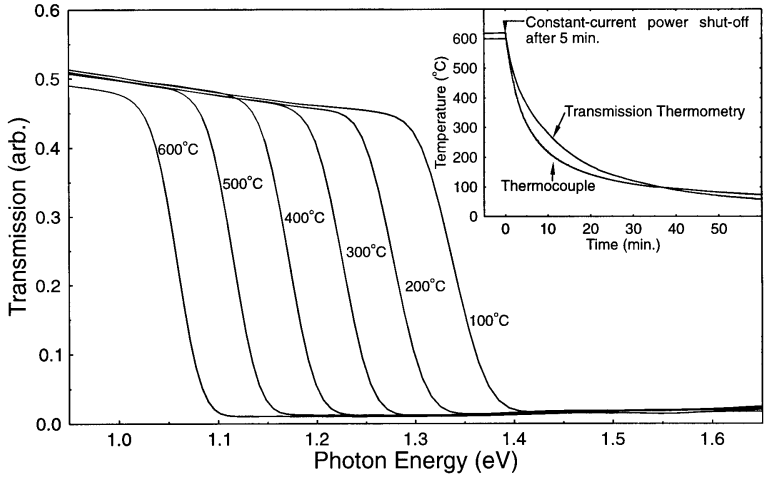

Fig. 2. Six transmission curves are shown as a function of photon energy. Each curve was taken after the substrate temperature remained unchanged for more than 30 min, while being heated with a constant current supply. The sharp drop in the transmission spectra occurs once the photon energy is large enough to cause band-to-band transitions. (inset) The thermocouple temperature, and the transmission thermometry calculated temperature are shown as a function of time. A constant current power supply maintained a wafer temperature of 600°C (thermocouple read 615°C) for five minutes. After which the current was set abruptly to zero. This data shows that the dynamic response is very different for the thermocouple and substrate.

substrate heater is turned off, the substrate temperature can still be accurately measured. Thus, the cooling rate can be accurately determined. It is surprising to find that the thermocouple temperature dropped much faster than the temperature of the substrate, as shown in the inset in Fig. 2. After holding the substrate at 600°C for five minutes (thermocouple reads 15°C higher), the power to the substrate heater was set to zero. The thermocouple reached 250°C in about 7 minutes, while the substrate required about 12 minutes. Often a heterostructure requires growths of different materials be carried out at different temperatures. Using the thermocouple as a gauge of the response time for the substrate to change temperatures may not be accurate. If a particular layer has a narrow temperature window for high-quality deposition, then starting the growth too soon could lead to a poorly defined structure.

Somewhat surprisingly we found that other sources of radiative heat (i.e. from an effusion cell) had a significant effect on the substrate temperature that was undetectable by the thermocouple. To demonstrate this, the power to the substrate heater was maintained at a constant value which gave a constant sample temperature of 580°C. Then, the shutter to the Si effusion cell, held at a temperature of 1300°C, was opened. During the $\sim$ 3 min. the shutter was opened, the substrate temperature was measured by both the thermometry system and thermocouple and displayed in Fig. 3. Surprisingly, the substrate temperature is seen to experience $\sim$ 12°C increase in temperature, while the thermocouple temperature remained constant. The substrate returned to 580°C when the Si shutter was closed. We believe the increase in temperature is due to the sample

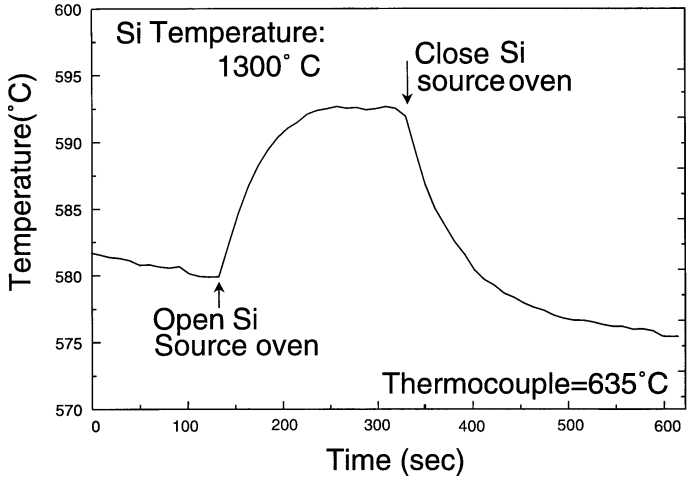

Fig. 3. Transmission thermometry temperature plotted versus time while opening the shutter to the Si effusion cell. A constant current power supply maintained a wafer temperature of 580°C. Therefore, the increase in sample temperature is do the radition emmitted from the Si cell which is at 1300°C. Interestingly, the thermocouple temperature remained constant while the Si shutter was opened.

absorbing the radiative heat from the Si effusion cell. Again, this temperature increase may be adversely effecting the deposition quality during the growth process.

One drawback for our system is that we can only measure the substrate temperature at the center of the substrate. We would need to install multiple quartz rods across the backside of the wafer to measure the temperature at other points on the wafer. It is known that a temperature gradient can occur between the center of the wafer and the edge of the wafer. With our measurement system we cannot determine this gradient. Another disadvantage of this optical detection system, is that is does require that one install components inside the MBE machine.

In summary, the key advantage of incorporating the optical transmission temperature measurement system into our MBE chamber is fast and accurate temperature determinations which are derived from a fundamental optical property. Thus, our temperature knowledge is not subject to variations due to different substrate mounting strategies or even which MBE machine is used to perform the measurement. This system has provided the most accurate means to measure the substrate temperature within an UHV chamber to date and significantly impacted our experimental capabilities.

3. Atomic Structure of the GaAs(001)-(2×4) Reconstructed Surface

3.1. *Proposed structural models for GaAs*(001)-(2 × 4)

The 2 × 4 reconstruction of the GaAs(001) surface is the reconstruction upon which device structures are fabricated. Thus, knowing the periodic atomic arrangement of this reconstruction is both of technological and fundamental importance. Consequently, over the past decade state-of-the-art techniques from both theory and experiment have focused on uncovering the atomic structure of this surface.[5,7,13,16,20–22,35–39] The γ, β, $\beta 2$ and α are four different structural models for the GaAs(001)-(2×4) surface, which have been extensively debated and shown in Fig. 4(a)–(d), respectively. Intensity differences in the fractional order spots in the reflection high-energy electron diffraction (RHEED) patterns were used to identify

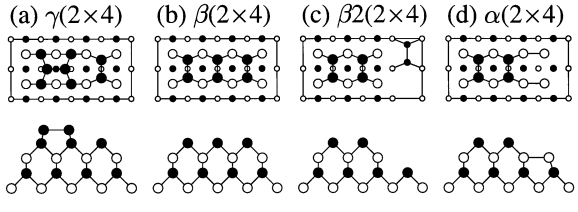

Fig. 4. Four proposed structural models of the GaAs(001)-(2 × 4) surface reconstruction. Each model shows two views, top (above) and side (below), and the names given to the structural model is indicated in the figure. Filled, and empty circles represent As, and Ga, respectively. Larger circles represent atoms closer to the surface.

the structure of three (2×4) phases: γ, β, and α, prepared under different growth conditions.[35] However, changes in RHEED spot intensities may also arise from disorder rather than a periodic structural change in the unit cell. This motivated local real-space scanning tunneling microscopy (STM) experiments of differently prepared GaAs(001)-(2×4) surfaces, which observed structures consistent with both two and three As-dimer models.[7,22,38] More recently, STM experiments of these three phases suggest that they all have the same unit cell structure, one with two top layer As-dimers, such as the α or $\beta 2$.[13,20] Theoretical modeling concluded that the α and $\beta 2$ structures have the lowest formation energy and the $c(2 \times 8)$ variety of the $\beta 2$ structure is the most favorable.[5,12,21]

Ideally, the atomic structure of the most well-ordered GaAs(001)-(2×4) surface is desired. Recent *in situ* grazing incidence X-ray diffraction measurements of a well-ordered surface have observed a structure that is in agreement with the $\beta 2$ model.[16] In this section, the atomic structure of the well-ordered GaAs(001)-(2×4) surface is determined using a combination of real-space STM images and first-principles density-functional theory.[28]

3.2. *Experimental and theoretical investigations*

The experiments were carried out within an ultrahigh vacuum (UHV) multi-chamber facility ($5–8 \times 10^{-11}$ Torr throughout) which contains a molecular beam epitaxy (MBE) chamber (Riber 32P) connected *in situ* to a surface analysis chamber, which contains an Omicron STM.[27] The MBE system includes a substrate temperature determination system that is accurate to $\pm 2°$C as discussed in Sec. 2.[26] In addition, the MBE system includes a reflection high-energy electron diffraction (RHEED) system for real-time surface characterization.

The substrate wafers used were commercially available, "epi-ready", $n +$ (Si doped $10^{18}/\text{cm}^3$) GaAs(001) $\pm 0.1°$ substrates. The wafers were loaded into the MBE system without any chemical cleaning and the surface oxide layer was removed and a 1.5-μm-thick GaAs buffer layer was grown at 580°C using a growth rate of 1.0 μm/h as determined by RHEED oscillations and an As_4 to Ga beam equivalent pressure (BEP) ratio of 15. Then, the substrate was annealed at 600°C, with an As_4 BEP of 1.0 μTorr for 15 min. and then at 570°C, with the same As_4 BEP for an additional 15 min. After this, the sample was cooled to 450°C at a rate of 1.5°C/s while simultaneously ramping the As_4 BEP to zero by the time the sample reached 500°C. The sample was held at 450°C for 15 min. to allow the As_4 to be pumped out of the chamber. Finally, the sample was cooled at a rate of 1.5°C/s to room temperature, transferred to the STM without breaking UHV, and imaged at room temperature.

To compare with the STM images, simulated STM images were extracted from density functional calculations without modeling the STM tip. These calculations were performed within the local-density approximation by employing a plane-wave-pseudopotential approach with a cutoff energy of 10 Ryd.[40] The GaAs(001) surface was modeled as a seven-layer slab followed by a vacuum region larger than 2 nm. The

bottom layer of atoms was passivated with pseudo-hydrogen atoms and kept fixed, while the top six layers were relaxed until all the forces were less than 0.5 eV/nm. After structural relaxation, extracting isocontour surfaces of a suitably defined local density of states generated numerically simulated constant current STM images. The local density of valence band states were integrated from the valence band minimum (VBM) to 0.3 eV and 1.1 eV below the VBM. This mimics the range of filled-state sample biases used in the STM images, which are referenced with respect to the Fermi level of the sample located in the middle of the 1.4 eV surface band gap.[11]

3.3. *Determination of the structural model for the well ordered surface*

A filled-state STM image of the GaAs(001)-(2×4) reconstructed surface (11 nm$\times$ 11 nm) taken with a sample bias of -2.1 V is shown in Fig. 5(a). The multiple bright rows, running diagonally across the image, have a center-to-center distance of 1.6 nm along the [110] direction, representing the "4-by" periodicity of the (2×4) reconstruction. Along the $[1\bar{1}0]$ direction another oscillation in the gray level occurs at twice the spatial frequency or every 0.8 nm representing the "2-by" periodicity of the (2×4) reconstruction. These "2-by" features are topographically flat and have an overall width of ~ 0.9 nm along the [110] direction. These features indicate that the top layer structure consists of two dimers of equal height as depicted by the two ball-and-stick dimer models drawn over the STM image in Fig. 5(a). This is inconsistent with the γ model [cf. Fig. 4(a)] which would have an additional As dimer on top of the row. It is also inconsistent with the β model [cf. Fig. 4(b)] which would have a feature spanning over $\frac{3}{4}$ of the length of the "4-by" width.

The structure within the trenches between the top layer As-dimer rows is also resolved in Fig. 5(a). The periodicity of the trench structure is 0.8 nm along the $[1\bar{1}0]$ direction, similar to the "2-by" periodicity of the top layer dimer rows. However, this trench periodicity is shifted out of phase with the "2-by" periodicity of the top layer dimer rows, indicated by the white line and the three ball-and-stick As dimers drawn over the data. This shift is inconsistent with the α model, which has a symmetric arrangement of atomic features between the trenches and the top layer [cf. Fig. 4(c)]. This shift and all the other observed features in Fig. 5(a) are in agreement with the $\beta 2$ model [cf. Fig. 4(d)].

A first-principles generated STM image of the $\beta 2(2 \times 4)$ structural model at a filled-state bias of 0.3 V below the VBM is displayed in Fig. 5(b) as a continuation of the STM data shown in Fig. 5(a). The simulated STM data assumes an infinitely sharp STM tip, providing more resolution than obtained experimentally. Nevertheless, excellent agreement between the two images is achieved. Namely, the width of the top layer "2-by" features along the [110] direction is reproduced. In addition, the relative shift between the top layer "2-by" features and the "2-by" features within the trenches is reproduced. This is indicated with the white line and

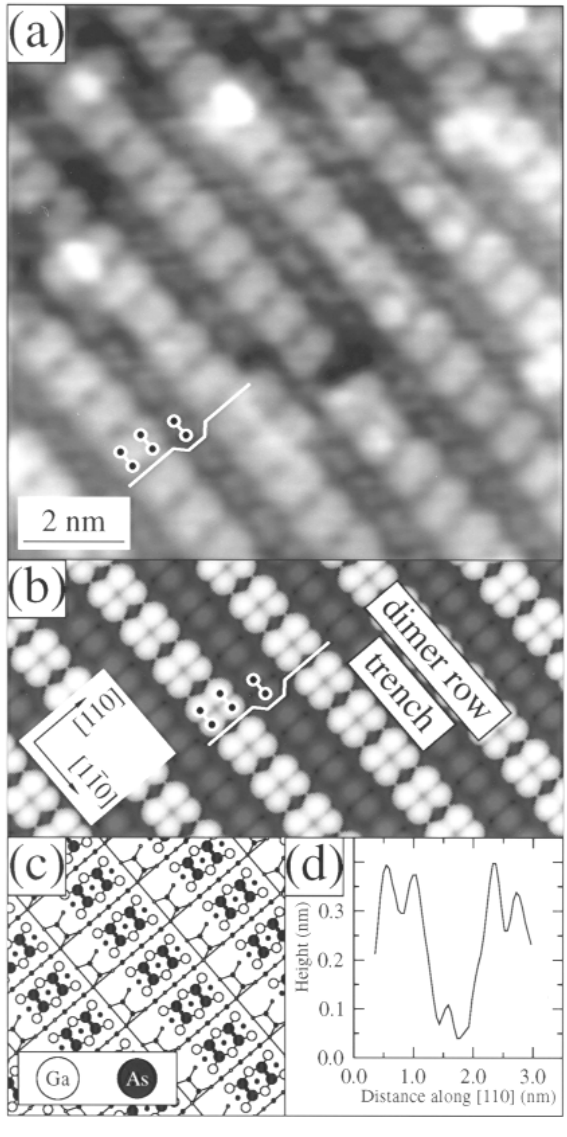

Fig. 5. (a) Filled-state STM image acquired with a sample bias of −2.1 V measuring 11 nm × 11 nm; (b) Simulated STM image of the $\beta 2$ structural model using a filled-state bias of 0.3 V below the valence band maximum; (c) $\beta 2$ structural model; (d) Height cross-section across a dimer trench along the [110] direction extracted from the STM image shown in (a).

the three ball-and-stick As dimers drawn over the simulated image. This point-by-point two-dimensional comparison of first-principles theory and STM data provides rigorous proof that the imaged surface has the same structure as the $\beta 2$ model. For clarity, a ball-and-stick $\beta 2$ structural model is drawn to scale in Fig. 5(c) as a continuation of Fig. 5(b).

A height cross-section taken along the [110] direction from the STM data displayed in Fig. 5(a) is shown as a line scan in Fig. 5(d). This height cross-section spans two top-layer dimer rows and the trench between them. This line scan shows that the topographic depth change that occurs between the dimer rows is ~ 0.3 nm, or a full monolayer (ML) height for GaAs(001).[41] This is in agreement with the $\beta 2$ model [cf. Fig. 4(c)] and in disagreement with the α model, which would show a height difference of only half a monolayer (0.14 nm) [cf. Fig. 4(d)].

3.4. *Uncovering a novel imaging mechanism —sample sharpening*

The features seen in the STM data and the agreement with the density functional theory conclusively point to the $\beta 2$ model as the correct structural model for this surface. Interestingly, however, the trench structure could only be resolved at the low sample biases as demonstrated in the nine (11 nm $\times$ 11 nm) STM images shown in Fig. 6. These images are of the same region of the GaAs(001)-(2 $\times$ 4) reconstructed surface and were taken at biases ranging from -3.0 V to -2.1 V as indicated. The location of the same feature in all the images is indicated by the white circle. Visible in these images are the top level As-dimer rows running diagonally in the $[1\bar{1}0]$ direction. In addition, the structure within the trenches

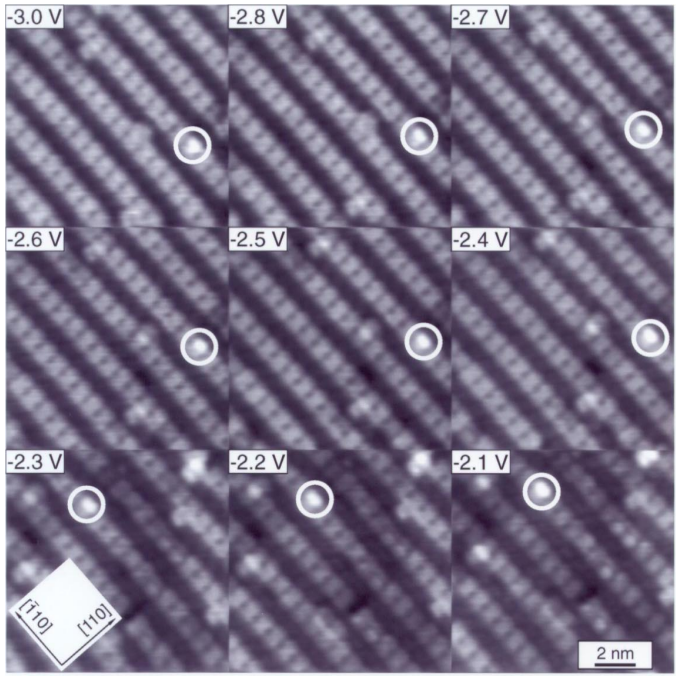

Fig. 6. Nine filled state STM images of the same measuring 11 nm $\times$ 11 nm region of the GaAs(001)-(2$\times$4) reconstructed surface. Sample biases range from -3.0 V to -2.1 V as indicated. The circle marks the location of the same feature in all the images.

first becomes visible when the sample bias is between −2.6 V – −2.4 V. The best visibility is from −2.3 V – −2.1 V.

To better contrast the bias dependent differences seen in these images a 2.8 nm × 4.4 nm section of the same region taken from both the −3.0 V bias image and −2.1 V bias image are shown in Fig. 7. The internal structure of the top layer "2-by" features is better resolved at the −3.0 V bias image. Namely, a distinct single minimum exists at the center of the top layer dimer row, indicating the presence of only two As dimers in the top layer and further supporting the $\beta 2$ model. This single minimum is less pronounced in the image taken of the same region but with a smaller sample bias of −2.1 V shown in Fig. 7(b). Most significantly, this smaller-bias STM image reveals the atomic structure within the trenches.

A bias-dependent feature in an STM image typically results from variations in the local density of states (LDOS) of the surface.[42] Interestingly, LDOS calculations for the As dimers in the trench reveal that there are a nearly uniform number of states available for tunneling at all filled state biases starting from the VBM. This rules out a change in the trench dimer's LDOS as a possible explanation for the observed bias dependence.

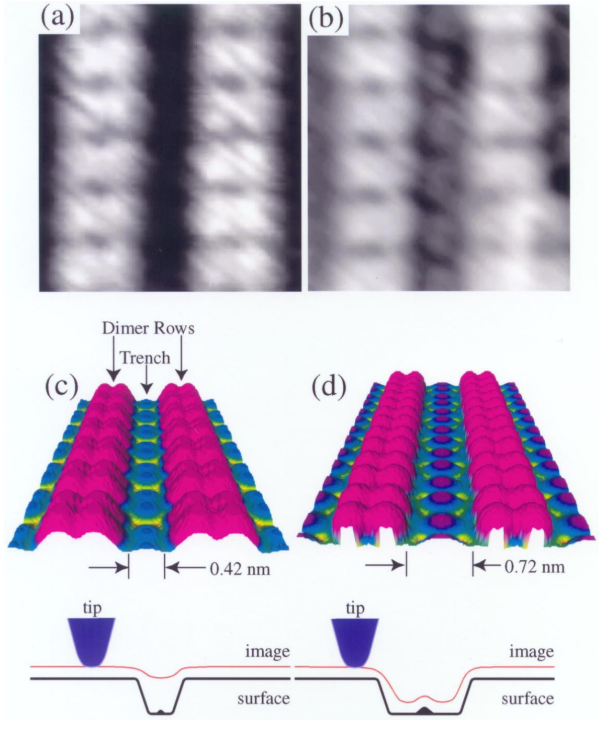

Fig. 7. (a) and (b) 2.8 nm × 4.4 nm filled-state STM images of the same area acquired with sample biases of −3.0 V and −2.1 V, respectively. (c) and (d) Simulated STM images using a filled-state biases of 1.1 V and 0.3 V below the valence band maximum, respectively.

The mechanism that explains this bias-dependent difference in the STM images was discovered after bias-dependent simulated STM images were produced. The simulated STM images taken at filled-state biases of 1.1 V and 0.3 V below the VBM are shown rendered in three-dimensions in Fig. 7(c) and 7(d), respectively. These images reveal a mammoth 0.3 nm increase in the physical width of the trench region as the filled-state bias is reduce by 0.8 V. This increase is monotonic, and is consistent with the monotonic change in the bias-dependent STM images. The trench widens as a result of the retracting surface of constant LDOS about the top layer As dimer dangling bond orbital. This retraction allows the STM tip to penetrate between the top-layer As dimer rows and image the As dimers within the trenches that are a monolayer (0.28 nm) lower. At larger biases, the narrower trench results in the tunneling current jumping from one top-layer As dimer to the next, missing the features in between. Thus, even though the As dimers within the trench have a uniform LDOS, at high biases those states are blocked by the orbitals of the top-layer As dimers.

An apt analogy for explaining the inability to image features within the trenches at larger biases is a geometric sample-tip convolution effect commonly seen in scanning probe microscopy.[43] However, geometric convolution effects do not disappear as the bias is lowered. In addition, they typically happen on length scales which are at least an order of magnitude or more larger than the 0.3 nm observed here. This new phenomenon can be described as an electronic sample-tip convolution effect. In this phenomenon, the step edge of the trench is sharper at smaller biases, and this electronic sample sharpening reduces the geometric tip-sample convolution, allowing the finite size tip to image inside the trench. This is a novel contrast mechanism and illustrated in the lower portion of Fig. 7.

In summary, all the atomic features of the GaAs(001)-(2 × 4) reconstructed surface have been resolved with STM and first principles density functional theory and conclusively point to the $\beta 2$ model as the correct model. Uncovering this structure required understating the novel sample sharpening STM contrast mechanism.

4. Spontaneous Island Formation

4.1. *Understanding the thermodynamic behavior of the spontaneously formed islands using the Ising model*

4.1.1. *Modeling the thermodynamics of surfaces*

Modeling the thermodynamics of the microscopic behavior of III–V surfaces is challenging due to their two-component nature. However, much success has been achieved using various techniques, such as: first-principles theory,[15] kinetic Monte-Carlo simulations,[44] rate equations,[45] and thermodynamics.[18] On single component surfaces, one of the oldest and simplest approaches to modeling is the celebrated two-dimensional (2D) lattice-gas Ising model.[46] Clever researchers have

been able to artificially create 2D systems with a fixed, sub-monolayer amount of one material deposited on a host surface made of a different material, and successfully applied the 2D lattice-gas Ising model.[47–51] These studies advance our understanding of phase transitions while illuminating the nature of interactions between atoms on surfaces, since the 2D Ising model has been theoretically studied in rigorous detail.[52,53] The above types of experiments are within the canonical ensemble (i.e. fixed number of particles) and therefore, they can fit their data to Onsager's exact solution similar to some 2D Ising-like magnetic phase transitions (i.e. fixed number of spins) that have been observed by neutron scattering.[54–56] The lattice-gas Ising model was originally framed within the more general context of the grand canonical ensemble, where the number of particles is free to fluctuate as it exchanges with a reservoir. This is unlike the ferromagnetic case where the number of spins is fixed. In this section, an experimental test of the general solution to the 2D lattice-gas Ising model within the grand canonical ensemble is presented on the GaAs(001) surface.

4.1.2. *Mapping out the density of islands versus the substrate temperature and As_4 pressure*

The relationship between the spontaneously formed islands, the substrate temperature, and As_4 flux was uncovered by preparing and imaging multiple samples in the MBE & STM system described in Sec. 3.2. Each sample was annealed for a fixed time (between 0.25–33 hrs.), a fixed temperature (between 500–700°C) and a fixed As_4 flux (between 0.01–10.0 μTorr), resulting in an exhaustive study of the accessible parameter space. To ensure the samples were in equilibrium, the anneal times were successively increased until the surface morphology remained unchanged, which resulted in 33 hour anneals for the lowest temperatures. After this, the sample was cooled to 450°C at a rate of 1.5°C/s while simultaneously ramping the As_4 BEP to zero by the time the sample reached 500°C. The sample was held at 450°C for 15 min. to allow the As_4 to be pumped out of the chamber. Finally, the sample was cooled at a rate of 1.5°C/s to room temperature, transferred to the STM without breaking UHV, and imaged at room temperature. For the latter two experiments, multiple filled-state STM images were acquired of various sizes using tips made from single crystal ⟨111⟩-oriented tungsten wire, a sample bias of −2.0–−3.0 V and a demanded tunneling current of 0.05–0.2 nA.

The thermodynamic behavior of both the lattice-gas and ferromagnetic Ising models was simulated as a function of temperature and fugacity[57] using Metropolis Monte-Carlo simulations[58] on a 2D lattice with 100×100 sites, or larger.

4.1.3. *The lattice-gas Ising model and the behavior of the spontaneous island formation*

The order parameters computed from Monte-Carlo simulation are shown in the lower half of Fig. 8. The order parameters are shown as a function of the reduced

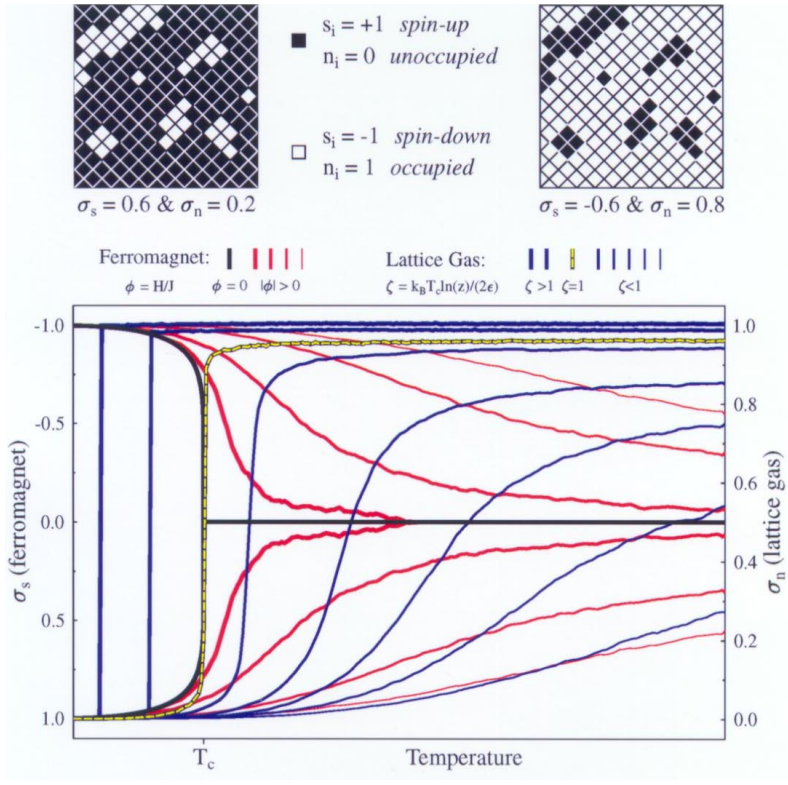

Fig. 8. Mapping of the 2D lattice-gas Ising model to the ferromagnetic model, and two possible real-space atomic configurations (above). Contrast in behaviors of the order parameters for the ferromagnetic, and lattice-gas Ising models (below).

parameters ϕ, and ζ, which span several decades ($\phi = H/J$, where H is the applied magnetic field strength, in units of energy, and J is the coupling energy between neighboring spins; $\zeta = k_{\mathrm{B}} T_{\mathrm{c}} \ln(z)/2\epsilon$, where k_{B} is Boltzmann's constant, T_{c} is the critical temperature, z is the fugacity and ϵ is the coupling energy between neighboring sites). The ferromagnet remains magnetized at high temperatures under large negative and positive magnetic fields and approaches the Onsager solution as the magnitude of the magnetic field approaches zero. In contrast, calculations for the lattice-gas system using the critical fugacity, $\ln(z_{\mathrm{c}}) = 2\epsilon/k_{\mathrm{B}} T_{\mathrm{c}}$ (i.e. $\zeta = 1$), show the density jumping from low to high occupation at T_{c} and not stopping at $\sigma_n = 0.5$. For fugacities greater than z_{c}, the density jumps from one side of the Onsager solution (lattice-gas coexistence curve) to the other as the temperature is increased. As the fugacity is decreased below z_{c}, the change in the density with temperature decreases, and stays low even for high temperatures. The contrast in behavior between the ferromagnetic and lattice-gas systems arises from the lattice-gas system being an open system, or within the grand canonical ensemble. In other

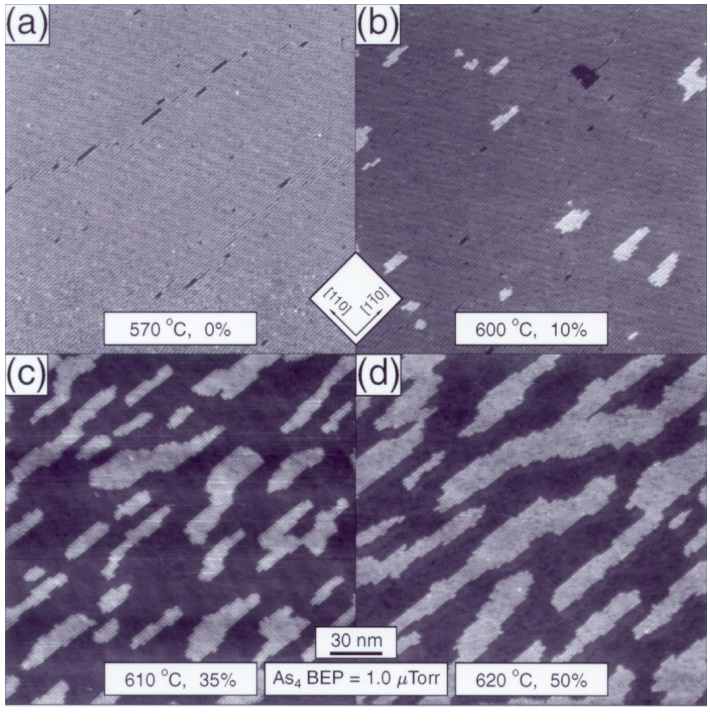

Fig. 9. Four 200 mm × 200 nm STM images of the GaAs(001)-(2 × 4) surface showing the spontaneous formation of islands. These samples were annealed under a 1.0 μTorr As_4 BEP at the temperatures indicated. Visible are the dimer rows of the 2 × 4 reconstruction running in the [1$\bar{1}$0] direction. The coverage of the islands is also indicated.

words, changing a site from unoccupied to occupied changes the energy not solely due to the change in its configuration with its nearest neighbors but also due to the mass that is added to the system. In contrast, flipping a spin from $-\frac{1}{2}$ to $\frac{1}{2}$ changes the energy solely due to the change in its configuration with its nearest neighbors.

All STM images show either a flat GaAs(001)-(2×4) reconstructed surface or one that has flat terraces covered by only one-monolayer-high (0.28 nm) GaAs islands as seen in Fig. 9. It has been determined that any one surface structure can be reversibly transformed into any other structure by annealing it at the corresponding temperature and As_4 flux. An STM image of a sample annealed at 560°C and 0.03 μTorr As_4 that shows the spontaneously formed islands on multiple terraces is displayed in Fig. 10(a), where each terrace is shown as a separate grey-level. Notice how the edge of each terrace affects the formation of islands by not allowing double-height steps to form. To minimize this influence on the analysis, 200 nm × 200 nm regions are cropped far from terrace edges as indicated by the dashed box on Fig 10(a). 10–20 of these smaller regions taken from 5–10 larger images are thresholded to compute the fractional coverage of the islands (cf. Fig. 8). The average fractional coverage is the order parameter and has a uniform standard

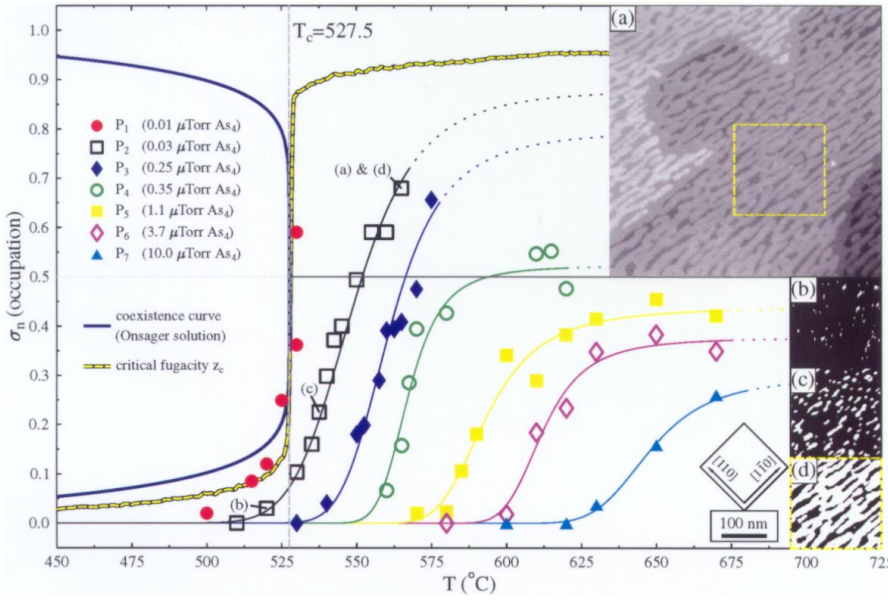

Fig. 10. The measured order parameters from the STM images as a function of temperature, and applied As_4 gas pressure as well as the coexistence curve and the curve of critical fugacity from the Monte-Carlo modeling. The lines drawn through the data are best fit Fermi functions. (a) 600 nm × 600 nm STM image showing the layout of the domains on multiple terraces. (b)–(c) 200 nm × 200 nm thresholded STM images. These STM images were annealed at the temperatures indicated on the 0.03 μTorr As_4 pressure series data.

deviation of $\sim 5\%$ for all the samples. Three thresholded 200 nm × 200 nm images are shown in Fig. 10(b)–(d), which visually demonstrates the increase in occupied area from 0.05 to 0.2 to 0.7, respectively with increasing anneal temperature under a constant 0.03 μTorr As_4 flux.

To better visualize the behavior of the measured order parameters, they are plotted versus temperature and also shown in Fig. 10. A best fit Fermi function is drawn over each series annealed under the same As_4 flux to highlight the trend of the data. The dashed lines indicate the experimentally inaccessible region. The series of samples annealed under the lowest As_4 flux of 0.01 μTorr has the sharpest increase in the density of the islands as a function of temperature. From this series the critical temperature, T_c is estimated to be $527.5 \pm 2°C$ and the coexistence curve (onsager solution) is plotted along with the critical fugacity curve from the Monte-Carlo simulations. The rest of the samples annealed under larger As_4 fluxes have higher onset temperatures for the order parameter, slower rates of increase, and saturate at lower coverages.

The STM images in Fig. 9(a)–(d) show that the domains are elongated in the $[1\bar{1}0]$ direction. This microscopic information is lost when solely monitoring the order parameter, but can be obtained from the microscopic structure by computing

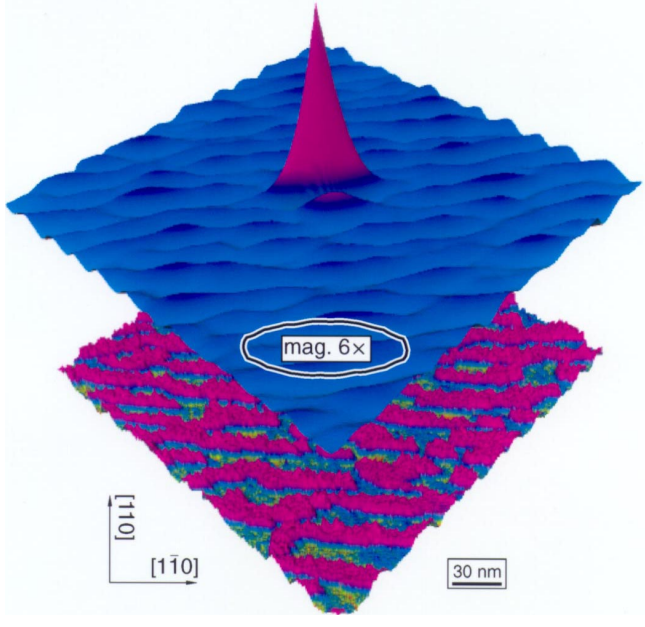

Fig. 11. Site–site correlation function (above) computed from the real-space domain structure STM image (below) for the sample closest to T_c with a coverage of 0.5. The inset displays the ellipse taken at $1/e$ of the maximum drawn to scale, but magnified 6×, with an aspect ratio of 3.0.

the site–site correlation function. The correlation function and the real-space domain structure of the sample closest to T_c with a density of 0.5 is shown in Fig. 11. The correlation function decays as a power law with distance from the center. The ellipse shown is taken at $\frac{1}{e}$ of the maximum and has an aspect ratio, AR, of 3.0.

4.1.4. *Microscopic view, asymmetric coupling energies, and critical exponents*

The behavior of the coverage obtained by *increasing* the As_4 flux by 3 orders of magnitude is similar to the Monte-Carlo results where the fugacity or pressure is *decreased* over ~ 3 orders of magnitude. This inverse relationship is expected, because earlier studies by Tersoff, Johnson, and Orr determined that the Ga adatom concentration or pressure is inversely proportional to the arsenic flux.[18,17] On an atomistic level, it is these Ga adatoms that are mobile on the surface at high temperatures, which are then frozen into GaAs islands when cooled to room temperature. The higher arsenic pressure results in terminating the gallium surface,[28] thereby lowering the number of mobile Ga atoms. This Ga adatom concentration is related to the Ga fugacity, which directly compares to the fugacity of the lattice-gas simulations. Ideally, an equation of state could be developed that relates the As_4 BEP, substrate temperature, and surface morphology from the data displayed in Fig. 10.

Table 1. Measured critical exponents with predicted 2D, and 3D values.

Quantity	Scaling law	Measure value	2D	3D
pair correlation function ($T = T_c$)	$G(r) \sim r^{-\eta}$	$\eta = 0.25 \pm 0.05$	0.25	$\sim$ 0.04
correlation length, $G(r, T < T_c) \sim r^{-\eta} e^{-r/\xi}$	$\xi \sim \lvert\frac{T}{T_c} - 1\rvert^{-\nu}$	$\nu = 1.0 \pm 0.25$	1	$\sim$ 0.638
critical isotherm ($T = T_c$)	$P - P_c \sim \lvert 2\sigma_n - 1\rvert^{\delta}$	$\delta = 15 \pm 3$	15	5
compressibility, $K_T(T < T_c) = \sigma_n^{-1}(\partial\sigma_n/\partial P)_T$	$K_T \sim \lvert\frac{T}{T_c} - 1\rvert^{-\gamma}$	$\gamma = 1.74 \pm 0.2$	1.75	1.25

The STM images of the 2D islands in Fig. 9 and Fig. 10(a)–(d), and the reduced macroscopic thermodynamic data in Fig. 10 provide strong evidence that this system follows the 2D lattice-gas Hamiltonian. However, quantifying a system's dimensionality and internal degrees of freedom requires the measurement of critical exponents.[59] Because of the large data set acquired as a function of temperature, pressure, coverage, and time an unprecedented *four* of the seven 2D universal critical exponents are determined and shown in Table 1 with their functional relationships. All seven exponents can be determined by measuring only two and their interrelationships can be tested by measuring more. The pair correlation critical exponent η, is a measure of the average domain size at the critical point. It is measured from the decay of the correlation function shown in Fig. 11, and our value is in good agreement with the 2D Ising prediction.

The correlation length critical exponent ν, is a measure of how the island size changes with temperature. It is calculated by extracting the width at $\frac{1}{e}$ of the maximum from the correlation functions as a function of temperature assuming that the Ga pressure is constant in the 0.01 μTorr series from 500 to 525°C. The isotherm critical exponent δ, is a measure of how quickly the coverage changes with pressure. It is calculated using pressure and coverage differences and ratios to eliminate unknown coefficients and assumes that the Ga pressure scales with the arsenic pressure from 0.25 to 0.01 μTorr at 530°C. Finally, the compressibility critical exponent γ, is a measure of how the compressibility changes with temperature. It is calculated using the 0.01 and 0.03 μTorr series of data between 515 and 525°C (note interpolated values for σ_n were used). This unprecedented large set of critical exponents, all well within the 2D Ising universality class, is the most rigorous testament to this system's 2D Ising behavior and was achievable because of the microscopic images obtained with STM.

Beyond being a study of a 2D Ising system, this study also demonstrates that the thermodynamics of the technologically important GaAs(001) surface can be understood with the Ising model. To complete this picture, the coupling energies in both the [110] and [1$\bar{1}$0] directions are needed. At T_c and z_c the system reduces to the zero-field Hamiltonian, where the coupling energies, $\epsilon_{[110]}$ and $\epsilon_{[1\bar{1}0]}$ and T_c are related by Onsager's[52] original finding:

$$\sinh\left(\frac{\epsilon_{[110]}}{2k_B T_c}\right)\sinh\left(\frac{\epsilon_{[1\bar{1}0]}}{2k_B T_c}\right) = 1\,. \tag{1}$$

Unfortunately, this equation has two unknowns which are the energy differences between an atom having a neighbor or not (or the binding energy at a step edge). One might naively assume that the aspect ratio of the islands is the ratio of the coupling energies, however this is not true. Fortunately, T. T. Wu *et al.*, calculated the exact correlation function for the 2D Ising model.[60] From that paper, this formula

$$\frac{\sinh(\epsilon_{[1\bar{1}0]}/2k_{\mathrm{B}}T_{\mathrm{c}})}{\sinh(\epsilon_{[110]}/2k_{\mathrm{B}}T_{\mathrm{c}})} = (AR)^2\,, \tag{2}$$

can be derived, where AR is the aspect ratio of the correlation function. Now, for the first time two equations exist relating the two coupling energies. For our system we find $\epsilon_{[1\bar{1}0]} = 250 \pm 25$ meV and $\epsilon_{[110]} = 45 \pm 5$ meV. These coupling energies are the energy cost for forming a step edge on the GaAs(001) surface, thus providing numerical values for testing against theoretical predictions.[61] This also explains why the islands are longer in the $[1\bar{1}0]$ direction. With absolute knowledge of the coupling energies the Hamiltonian is complete and one can solve for equilibrium and non-equilibrium properties using standard methods.[62]

In summary, the 2D lattice-gas Ising model within the grand canonical ensemble has been successfully applied to the technologically important GaAs(001) surface. Surprisingly, the single component Ising model can successfully describe a two component system, this is because the Ga atoms are the constituents and the arsenic pressure provides an external control of the Ga pressure. Modeling the GaAs(001) surface and developing an equation of state is possible with the complete knowledge of the 2D Ising Hamiltonian that is presented.

4.2. *Structure of the spontaneously formed islands*

The discovery of spontaneous island formation gave insight into the relationship between the arsenic pressure, the substrate temperature and the surface morphology framed within the lattice-gas Ising model. In addition, the geometry of the islands helped to uncover the step formation energies. However, how the island size and shape changes with temperature can give insight into the effect of strain on these islands.[63]

In this section, the equilibrium shape of spontaneously formed islands on the GaAs(001) surface are examined with STM. The observed behavior of the coverage of the islands with temperature is discussed in terms of fundamental thermodynamics. While, the shape and size of the islands is discussed in terms of differences in step formation energies and strain.

4.2.1. *Equilibrium shape of islands versus temperature and size*

The equilibrium morphology of the GaAs(001)-(2×4) surface is composed of flat terraces that are either covered or not covered with one monolayer (0.28 nm) high islands as displayed in the 1 μm $\times$ 1 μm STM images in Fig. 12. The images are

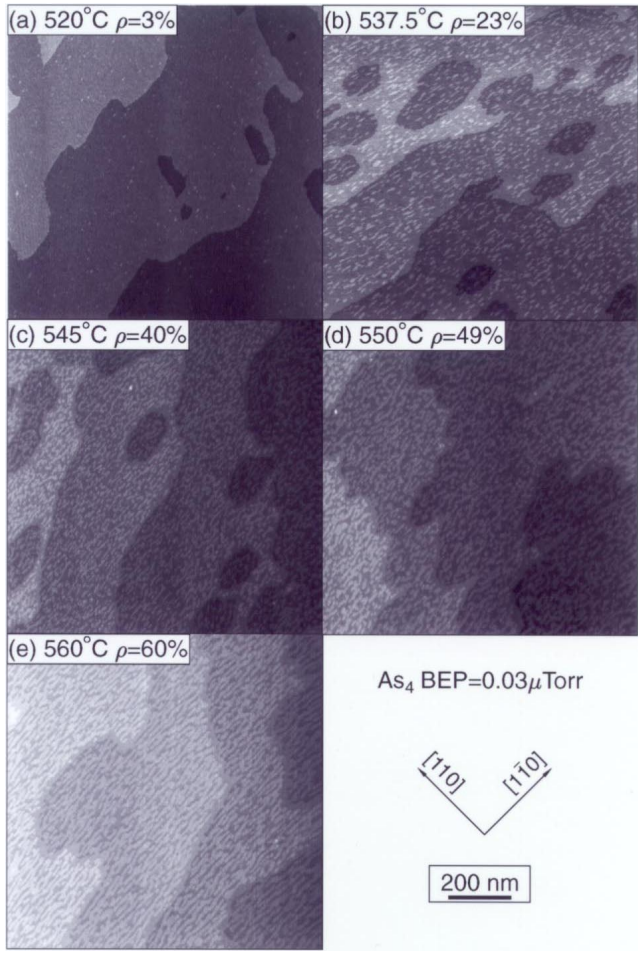

Fig. 12. Filled-state (3.0 V), 1 μm $\times$ 1 μm STM images showing the spontaneously formed islands created by annealing at the temperatures indicated, and under a 0.03 μTorr As_4 flux. The coverage, ρ increases with temperature, and all the islands are elongated in [1$\bar{1}$0] direction.

unprocessed, except for having a (001) plane subtracted from them which makes each terrace have a separate color separated by a 0.28-nm-high step. Notice how the island coverage increases as the substrate temperature increases. The islands are also elongated in the [1$\bar{1}$0] direction and tend to increase in size, yet maintain a constant aspect ratio with increasing temperature. In addition, the edge of each terrace affects the formation of islands by not allowing double-height steps to form.

The microscopic structure of the elongated monolayer-high GaAs islands is displayed in the 200 nm $\times$ 200 nm STM image in Fig. 13(a). This sample was annealed at 560°C, and shows a surface 60% covered with islands. The islands are well ordered and elongated. The thin white lines running diagonally in the [1$\bar{1}$0] direction

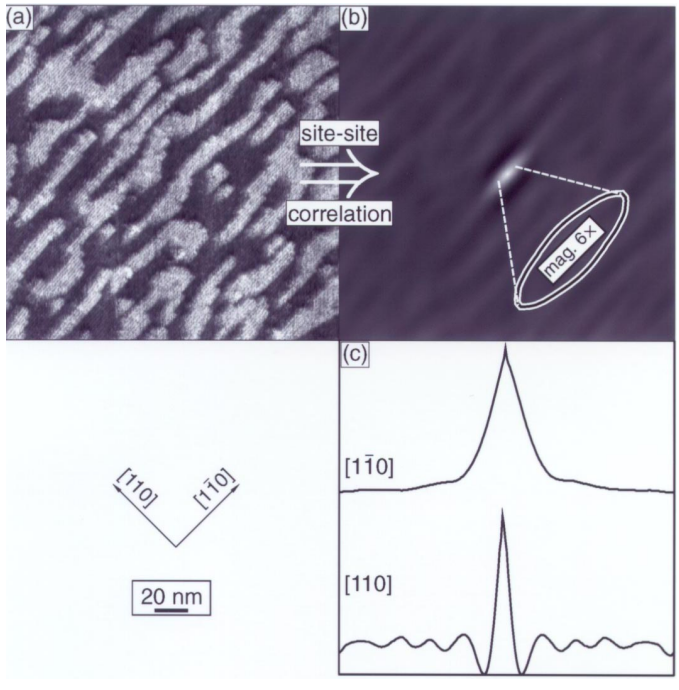

Fig. 13. (a) A 200 nm × 200 nm STM image of the spontaneously formed GaAs islands annealed at 560°C under an As_4 BEP of 0.03 μTorr, (b) A correlation function calculated from the same image (c) A line profile along [1$\bar{1}$0], and [110] directions.

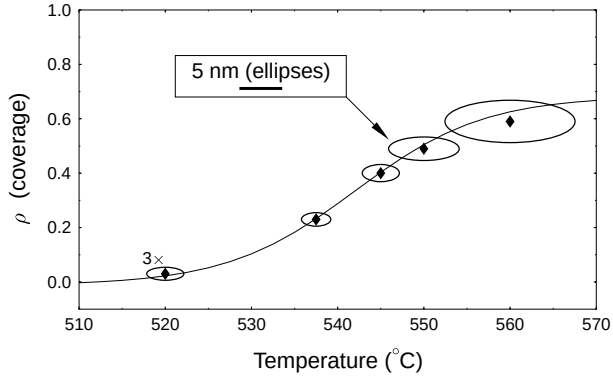

Fig. 14. Island coverage versus temperature (shown as diamonds). Ellipses are $1/e$ cuts from the correlation function, and are drawn with its center on the corresponding diamond.

on both the islands and terrace are separated by 1.8 nm in the [110] direction and result from the "4-by" periodicity of the (2 × 4) reconstruction.[28] To quantify the island geometry a site–site correlation function is computed from the STM image and displayed in Fig. 13(b). The correlation function is elongated in the same di-

rection as the islands and a cross-section taken at $1/e$ of the maximum is the ellipse shown in the inset with an aspect ratio of 3.0. Line profiles of the correlation function taken along the $[1\bar{1}0]$ and the [110] directions are displayed in Fig. 13(c) and show the contrast in the correlation length between the two directions.

The coverage is plotted versus anneal temperature for each sample and displayed in Fig. 14. This series of samples shows a Fermi-like functional relationship with temperature. To compare the different island geometry a correlation function was computed for each STM image and an ellipse was extracted at the $1/e$ point. A characteristic ellipse is plotted about the corresponding island coverage and anneal temperature point shown in Fig. 14. The ellipses get bigger with increasing temperature, however, the aspect ratio stays relatively constant, between 2 and 3, as the temperature is increased.

4.2.2. *Reasons for the asymmetry*

It may seem counterintuitive that the equilibrium morphology of the GaAs(001)-(2×4) reconstructed surface is composed of islands since the additional steps would raise the internal energy of the system due to the broken bonds at the edges. However, the island formation also increases the entropy of the system. Thus at high temperatures for certain systems where the broken bond energy is low island formation is favorable. We believe this is the driving force for the equilibrium island morphology of the GaAs(001)-(2×4) surface as described in Sec. 4.1.

The elongation of the islands is a direct consequence of the asymmetry in the energy cost to break a bond on different sides of an island. The GaAs(001) surface was successfully described using the 2D lattice-gas Ising model, where two explicit relationships between the energies and aspect ratio were presented.[29] By combing

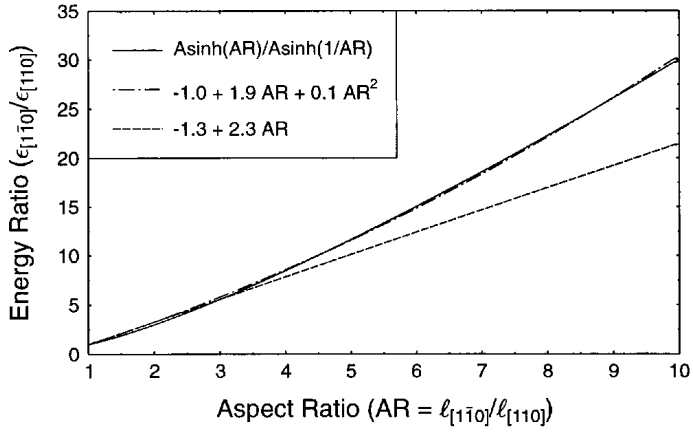

Fig. 15. Step formation energy ratio versus island aspect ratio. The exact 2D Ising model prediction is shown as a solid line. A linear approximation is shown as a dashed line. A quadratic approximation is shown as a dot-dashed line.

these relationships the following formula is predicted

$$\frac{\epsilon_{[1\bar{1}0]}}{\epsilon_{[110]}} = \frac{A\,\sinh(AR)}{A\,\sinh(1/AR)}\,. \tag{3}$$

as the relationship between the aspect ratio, AR and the energy ratio of the bond strengths in the two directions $\epsilon_{[1\bar{1}0]}/\epsilon_{[110]}$.[29,64,65,60] This result is plotted as a solid line in Fig. 15. For an aspect ratio of unity an energy ratio of unity is predicted, as one would expect. Using our experimentally determined aspect ratio of 3 it predicts an energy ratio of 5.6. A linear approximation to these two points from Eq. (3) is displayed as a dashed line in Fig. 15. This approximation is commonly used in the literature and sometimes referred to as a Wulf approximation. Notice that it deviates quickly from Eq. (3) for aspect ratios greater than 3.5. A quadratic approximation to Eq. (3) is displayed as a dot-dashed line in Fig. 15. This approximation is simpler than Eq. (3) and is a good fit. One can compare island shape as a function of island size with recent theoretical work by Li *et al.*[63] Li's study shows that the shape of the islands should change with size if there is a significant amount of strain anisotropy. Our finding that the aspect ratio stays relatively constant as the size increases indicates that the strain effects are not significant.

Independent of why these islands form and their size and shape, this phenomenon is remarkable and potentially useful. An ongoing debate in the optical and electrical properties of reduced dimensionality systems is to determine what is the explicit role of interface roughness. It is now possible to produce interfaces with systematically varying nanoscale roughness with a well-defined correlation function to test these issues.

In summary, the temperature of the GaAs(001)-(2×4) reconstructed surface controls the size and coverage of the spontaneously formed islands. We find the islands shape is constant with an aspect ratio of three and predict an energy ratio of 5.6. This energy difference explains why the islands are elongated in the $[1\bar{1}0]$ direction. This knowledge may prove useful in producing interfaces with a tuneable amount of roughness.

5. Enabling Electron Diffraction to Determine Substrate Temperature and *Aperiodic* Surface Morphology

5.1. *Prior successes in electron diffraction of the GaAs*(001) *surface*

Simply put, the ability to deposit one high-quality single-crystal material on top of another allows fabrication of GaAs based heterostructures. A significant leap forward in the quality of the deposited layers came with the introduction of *in situ* electron diffraction.[66] Initially, it was used to uncover the periodic properties of the surface atomic structure.[67,68,6] Later on, the peak intensities were found to oscillate in time during growth which allowed measurement of the rate material was being deposited.[4] As the understanding of the relationship between the atomic-scale

surface morphology and the diffracted electrons has grown, so has the quality and capabilities of the growth process.[8,23] The complex nature of the growth process can still benefit from further refinements in the understanding of the relationship between the diffraction pattern, the surface morphology, the substrate temperature, and the elemental flux.

The III–V(001) surfaces exhibit a plethora of surface reconstructions, all with different stoichiometries and symmetries. Most of the well-ordered structures can be understood with thermodynamic models, indicating that the reconstructions are a fundamental property of the equilibrium state.[69] Specifically, first-principles theory calculations are routinely carried out, and tend to accurately reflect experimental observations.[28,70–72] Experimentally, the transitions between these reconstructions occur as a function of temperature and group-V flux. [73–75,35] Determining the precise temperature at which these transitions occur is problematic due to the temperature measurement schemes commonly employed in molecular beam epitaxy (MBE) systems. For example, differences as great as 140°C between the actual temperature and the thermocouple (TC) derived temperature have been observed.[31] To mitigate this problem, a common practice for the GaAs(001) surface is to calibrate the TC to read 580°C when the oxide is first removed. Even though this procedure is transferable from lab-to-lab, it can be performed only at one temperature and only at one particular time. In this section, the ability to use electron diffraction as an *in situ* tool to measure the substrate temperature as well as to determine the aperiodic surface morphology is presented.

5.2. *Mapping out the reconstruction transitions on the GaAs*(001) *surface*

The experiments were carried out in the combined MBE–STM facility described in Sec. 3.2. The RHEED measurements were performed on commercially available, "epi-ready", *n*-type (Si doped $10^{18}/\text{cm}^3$) 2-inch GaAs(001) $\pm 0.05°$ substrates that were loaded into the MBE system without any chemical cleaning. The surface oxide layer was removed at 590°C while exposing the surface to a 10 μTorr As_4 beam equivalent pressure (BEP) from a solid-source valve-controlled cell. A 1.5-μm-thick GaAs buffer layer was grown at 580°C using a growth rate of 1.0 μm/h as determined by RHEED oscillations, and an As_4 to Ga BEP ratio of 15. After growth, the surface was annealed under an As_4 BEP of 1 μTorr for 15 min. at 600°C followed by another at 570°C under the same conditions. This procedure improves the RHEED pattern and prepares the surface for RHEED measurements. Surface reconstructions for a fixed As_4 BEP were identified by either heating or cooling the substrate in 10°C increments, waiting 15 minutes, and recording the RHEED pattern in the [110], [1$\bar{1}$0], and [100] directions. This procedure was repeated for five different As_4 BEPs by adjusting the valve position on the arsenic cell. In addition, the RHEED patterns were measured without any As_4 BEP. This was done by first creating a $c(4 \times 4)$ pattern at low temperatures and low As_4 BEPs. Then, the As_4 BEP was eliminated which leaves the surface with a $c(4 \times 4)$ symmetry. By holding the

substrate temperature below 350°C, with no As_4 BEP for 30 min., the background As_4 was removed from the chamber by the ion pump. RHEED patterns were then recorded in 10°C increments as described above.

The STM measurements used identical but smaller substrates, the oxide was removed, a buffer layer was grown, and the surface was prepared as in the RHEED experiments. After preparation, the sample was then annealed at a desired As_4 BEP and temperature condition. While quenching to room temperature at 1.5°C/s, the RHEED pattern was monitored to ensure it did not change. The sample was then transferred to the STM without breaking UHV and imaged at room temperature. To confirm the high-temperature annealing procedure produced a sample that had reached equilibrium, the anneal times were successively increased until the surface morphology, as viewed with STM, remained unchanged ($\sim$ 10 min.). For the equilibrated samples, multiple filled-state STM images were acquired using tips made from single crystal ⟨111⟩-oriented tungsten wire, a sample bias of −3.0 V and tunneling current between 0.05–0.2 nA.

5.3. *Reconstruction map and spontaneous island formation*

Pressure and temperature conditions for the transitions between various surface reconstructions as observed by RHEED are shown in Fig. 16. Increasing the substrate temperature at any nonzero As_4 BEP results in the surface reconstruction

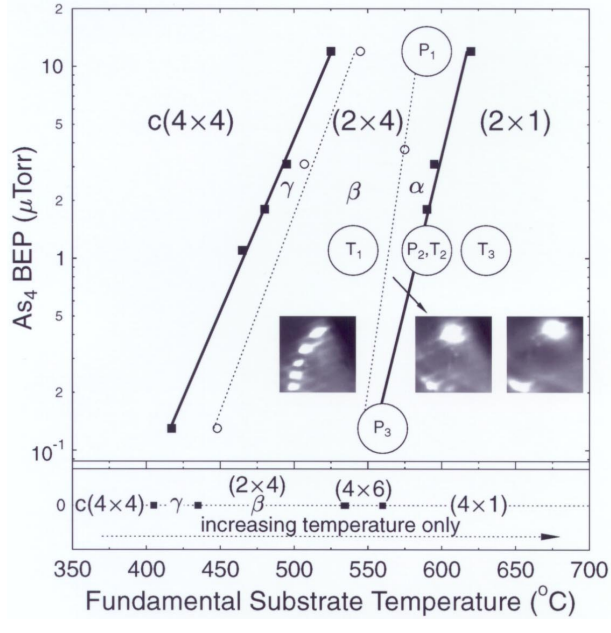

Fig. 16. RHEED-derived transition pressures (As_4 BEP) and temperatures for the GaAs(001) surface reconstructions. The lines are drawn as a guide to the eye.

changing from the $c(4 \times 4)$ to the (2×4) to the (2×1), as indicated by the solid lines. Decreasing the substrate temperature reverses the reconstruction sequence at the same temperatures. Within the (2×4) phase, three separate RHEED patterns were identified as the α, β, and γ sub-phases, and the transitions between these are identified with dashed lines. The β sub-phase RHEED pattern in the "4-by" direction consists of a specular, 1/4, 1/2, 3/4, and primary-order spots from top to bottom all with equal intensity, as illustrated by the photograph displayed in the region labeled β.[35] The α sub-phase pattern, is similar to the β except the 1/2-order spot is missing, as also illustrated in Fig. 16.[35] A characteristic (2×1) RHEED pattern in the "1-by" direction is also shown. The zero As_4 BEP data series is displayed on a separate graph directly below the logarithmic plot. The transition temperatures are marked with solid squares, and they happen only when the substrate temperature is increased from the $c(4 \times 4)$ phase. The pattern then changes to the (2×4) the (4×6), and finally to the (4×1).

Characteristic 1 μm $\times$ 1 μ m STM images of the morphology of the GaAs(001) surface are shown in Fig. 17. The labels for each image also mark the location on the RHEED reconstruction diagram (cf. Fig. 16) where the anneal occurred. The "T" labels represent an increasing-temperature, constant-pressure (constant As_4 BEP) data set through the β, α, and (2×1) phases, while the "P" labels represent decreasing-pressure, constant-temperature data set also through the three phases. The images are displayed in gray-scale, and unprocessed except for having a (001) plane subtracted from them to make each terrace a distinct color separated from the other by a 0.28-nm-high step. The trend in all the images is that the coverage of the islands increases with either increasing temperature or decreasing pressure. The lowest temperature and highest pressure annealing conditions produce a β sub-phase RHEED pattern, and a surface with large well-ordered terraces free of islands, as shown in Fig. 17 T_1 & P_1. The temperature-pressure condition that produces the α sub-phase RHEED pattern shows a surface with 10% of each terrace covered with one monolayer high GaAs islands, as shown in Fig. 17 T_2 & P_2. These islands have spontaneously formed on the surface due to annealing (i.e. without depositing any material from the gallium effusion cell).[29] The pressure-temperature conditions that produces a (2×1) RHEED pattern shows a surface with even more islands, as shown in Fig. 17 T_3 & P_3. Here, the surface roughness due to spontaneous island formation is so great that it is difficult to identify the original terraces. Notice, the islands still favor elongation in the $[1\bar{1}0]$ direction, and they avoid forming double height steps.

5.4. *Determining substrate temperature and aperiodic surface morphology a union of the real-space and reciprocal space view*

One of the most difficult problems within the MBE community is sharing knowledge of the substrate temperature for successful growth algorithms. This is due to poor

lab-to-lab reproducibility in the thermocouple and pyrometer methods of substrate temperature determination.[31,26] It is possible to use *in situ* RHEED to measure the substrate temperature by referencing the RHEED diagram shown in Fig. 16. This can be accomplished using one of two methods. First, holding the thermocouple derived substrate temperature fixed and adjusting the As_4 BEP until a transition [e.g. $c(4 \times 4)$ to (2×4)] is observed. Then, by knowing the As_4 BEP at which the transition was observed the true substrate temperature can be read off the diagram in Fig. 16 and used to calibrate the thermocouple temperature. Alternatively, one

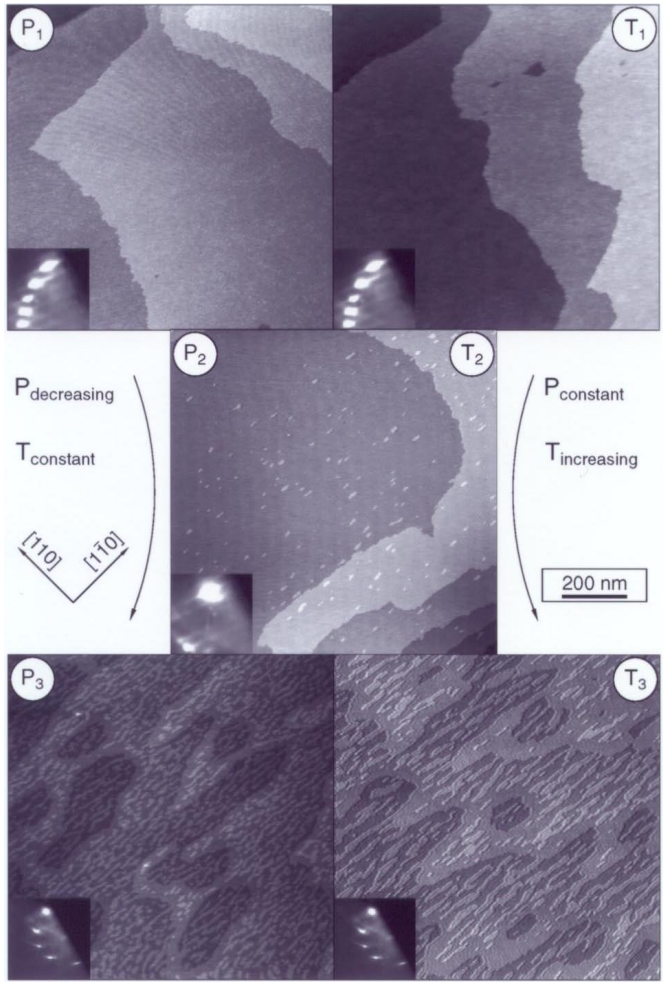

Fig. 17. 1 μm $\times$ 1 μm filled-state STM images taken at a sample bias of -3.0 V. The images labeled T_1 to T_3 represent an increasing-temperature, constant-pressure data series, while the images labeled P_1 to P_3 represent a decreasing-pressure, constant-temperature data series. The pressure-temperature annealing conditions for the STM samples are cross-referenced in the RHEED diagram shown in Fig. 16.

can hold the As_4 BEP fixed and adjust the thermocouple-derived substrate temperature until a transition is observed. Using the surface reconstruction transition method provides a large dynamic range, since the RHEED diagram has a transition at any temperature between 400–600°C. In addition, this method of substrate temperature determination is not subject to lab-to-lab variations, since the reconstruction transitions are independent of the substrate properties, such as dopant type and concentration.[76,12,70] In fact, we speculate that the only requirement is that ~10 ML of single crystal GaAs(001) be present. This methodology can be carried out on other III–V(001) surfaces, as well.[77]

Not only can RHEED be used for determining the substrate temperature, it can also be used to monitor the aperiodic surface morphology. The STM images indicate the β to α RHEED transition is coincident with spontaneous island formation. That is, when a β pattern is present at low temperatures the surface is flat, while when an α pattern is present at low temperatures the surface is covered with 2D GaAs islands.[29] We believe the rapid cool down procedure does not affect the surface. The concentration of islands and their geometry can be tuned and the process is reversible. Therefore, it is possible to use *in situ* RHEED to control the surface morphology by referencing the RHEED diagram shown in Fig. 16. This can be accomplished using one of two methods. First, increasing the substrate temperature while holding the As_4 BEP constant increases the island coverage. Alternatively, decreasing the As_4 BEP while holding the substrate temperature constant also increases the island coverage. This capability makes it possible to engineer interfaces with a tunable amount of roughness. Consequently, it may be possible to systematically study the role of interface roughness on transport or optical properties in reduced-dimensionality structures.[78]

Typically, diffraction patterns are used to predict atomic structural models simply from their symmetry. The $c(4 \times 4)$, (2×4), and (4×6) symmetries have been successfully modeled in this way. Interestingly, the other symmetries presented, namely the (2×1) and (4×1), have not been successfully modeled. In fact, it is believed that any structure with a "1-by" feature would violate the electron counting model.[71] In these structures it is believed that disorder is dominating the RHEED properties.[79] Nevertheless, little theoretical work has been done to understand the role of disorder on RHEED. A prescription for producing surfaces with a well known and tunable amount of disorder now exists for use as a test bed for such theory. These effects may play an important role in understanding the β to α RHEED transition, and possibly aid in understanding the general influence of disorder on diffraction.[16]

In summary, an algorithm for using RHEED on the GaAs(001) surface to determine the substrate temperature is presented. This method can be used in MBE machines even if they do not have access to a transmission thermometry system or on samples which are heavily doped or indium mounted. We believe this capability will aid in the lab-to-lab transfer of successful growth procedures. In addition, an algorithm for using RHEED to prepare a surface with a tunable amount of roughness

is presented. We believe this capability may lead to a better understanding of the relationship between the interface roughness and the optical and transport properties in confined structures, as well as aid the understanding of the role of disorder on diffraction.

Acknowledgments

This work was supported by the Office of Naval Research (ONR) under Grant No. N00014-97-1-1058, by the National Science Foundation under Grant No. DMR-9733994 and the C-SPIN MRSEC Grant No. DMR-0080054, and by the Research Corporation under grant No. RI0153.

References

1. A. Y. Cho, *J. Appl. Phys.* **42**, 2074 (1971).
2. A. Y. Cho, *J. Vac. Sci. Technol.* **8**, S31 (1971).
3. C. T. Foxon and B. A. Joyce, *Surf. Sci.* **64**, 293 (1977).
4. J. H. Neave,B. A. Joyce, P. J. Dobson and N. Norton, *Appl. Phys.* **A31**, 1 (1983).
5. D. J. Chadi, *J. Vac. Sci. Technol.* **A5**, 834 (1987).
6. R. Ludeke, *IBM J. Res. Dev.* **22**, 304 (1978).
7. D. K. Biegelsen, R. D. Bringans, J. E. Northrup and L. E. Swartz, *Phys. Rev.* **B41**, 5701 (1990).
8. J. Sudijono *et al.*, *Phys. Rev. Lett.* **69**, 2811 (1992).
9. W. G. Schmidt, *Appl. Phys.* **A65**, 581 (1997).
10. J. A. Stroscio, D. T. Pierce and R. A. Dragoset, *Phys. Rev. Lett.* **70**, 3615 (1993).
11. M. D. Pashley, K. W. Haberern, R. M. Feenstra and P. D. Kirchner, *Phys. Rev.* **B48**, 4612 (1993).
12. J. E. Northrup and S. Froyen, *Phys. Rev. Lett.* **71**, 2276 (1993).
13. T. Hashizume, Q. K. Xue, A. Ichimiya and T. Sakurai, *Phys. Rev.* **B51**, 4200 (1995).
14. M. Wassermeier *et al.*, *Phys. Rev.* **B53**, 13542 (1996).
15. A. Kley, P. Ruggerone and M. Scheffler, *Phys. Rev. Lett.* **79**, 5278 (1997).
16. Y. Garreau *et al.*, *Phys. Rev.* **B54**, 17638 (1996).
17. M. D. Johnson *et al.*, *Surf. Sci.* **350**, 254 (1996).
18. J. Tersoff, M. D. Johnson and B. G. Orr, *Phys. Rev. Lett.* **78**, 282 (1997).
19. A. I. Shkrebtii *et al.*, *Phys. Rev. Lett.* **81**, 721 (1998).
20. A. R. Avery *et al.*, *Phys. Rev. Lett.* **76**, 3344 (1996).
21. N. Moll, A. Kley, E. Pehlke and M. Scheffler, *Phys. Rev.* **B54**, 8844 (1996).
22. L. Broekman *et al.*, *Surf. Sci.* **331–333**, 1115 (1995).
23. W. Braun, L. Daweritz and K. H. Ploog, *Phys. Rev. Lett.* **80**, 4935 (1998).
24. Q.-K. Xue, T. Hashizume and T. Sakurai, *Prog. Surf. Sci.* **56**, 1 (1997).
25. Q.-K. Xue, T. Hashizume and T. Sakurai, *Appl. Surf. Sci.* **141**, 244 (1999).
26. P. M. Thibado, G. J. Salamo and Y. Baharav, *J. Vac. Sci. Technol.* **B17**, 253 (1999).
27. J. B. Smathers *et al.*, *J. Vac. Sci. Technol.* **B16**, 3112 (1998).
28. V. P. LaBella *et al.*, *Phys. Rev. Lett.* **83**, 2989 (1999).
29. V. P. LaBella *et al.*, *Phys. Rev. Lett.* **84**, 4152 (2000).
30. E. S. Hellman and J. S. Harris, Jr., *J. Cryst. Growth* **81**, 38 (1987).
31. B. V. Shanabrook *et al.*, *J. Vac. Sci. Technol.* **B11**, 994 (1993).

32. J. A. Roth, T. J. d. Lyon and M. E. Adel, *Mater. Res. Soc. Symp. Proc.* **324**, 353 (1994).
33. T. J. De Lyon, J. A. Roth and D. H. Chow, *J. Vac. Sci. Technol.* **B15**, 329 (1997).
34. J. A. Roth *et al.*, in *Indium Phosphide and Related Materials Conference Proceeding* (IEEE, New Jersey, 1997), p. 253.
35. H. H. Farrell and C. J. Palmstrom, *J. Vac. Sci. Technol.* **B8**, 903 (1990).
36. H. H. Farrell, J. P. Harbison and L. D. Peterson, *J. Vac. Sci. Technol.* **B5**, 1482 (1987).
37. M. D. Pashley *et al.*, *Phys. Rev. Lett.* **60**, 2176 (1988).
38. G.-X. Qian, R. M. Martin and D. J. Chadi, *Phys. Rev.* **B38**, 7649 (1988).
39. J. E. Northrup and S. Froyen, *Phys. Rev.* **B50**, 2015 (1994).
40. M. Bockstedte, A. Kley, J. Neugebauer and M. Scheffler, *Comput. Phys. Commun.* **107**, 187 (1997).
41. A monolayer (ML) of GaAs is 0.28 nm high, composed of a plane of both Ga and As and sometimes referred to as a bilayer.
42. R. M. Feenstra, J. A. Stroscio, J. Tersoff and A. P. Fein, *Phys. Rev. Lett.* **58**, 1192 (1987).
43. R. Wiesendanger, *Scanning Probe Microscopy and Spectroscopy, Methods and Applications* (Cambridge University Press, Cambridge, 1994).
44. M. Itoh *et al.*, *Phys. Rev. Lett.* **81**, 633 (1998).
45. M. D. Johnson *et al.*, *Phys. Rev. Lett.* **72**, 116 (1994).
46. T. D. Lee and C. N. Yang, *Phys. Rev.* **87**, 410 (1952).
47. M. J. Tejwani, O. Ferreira and O. E. Vilches, *Phys. Rev. Lett.* **44**, 152 (1980).
48. H. K. Kim and M. H. W. Chan, *Phys. Rev. Lett.* **53**, 170 (1984).
49. G. C. Wang and T. M. Lu, *Phys. Rev.* **B31**, 5918 (1985).
50. B. M. Ocko, J. X. Wang and T. Wandlowski, *Phys. Rev. Lett.* **79**, 1511 (1997).
51. D. Arndt, S. Fassbender, M. Enderle and K. Knorr, *Phys. Rev. Lett.* **80**, 1686 (1998).
52. L. Onsager, *Phys. Rev.* **65**, 117 (1944).
53. B. M. McCoy and T. T. Wu, *The Two-Dimensional Ising Model* (Harvard University Press, Cambridge, Massachusetts, 1973).
54. R. J. Birgeneau, H. J. Guggenheim and G. Shirane, *Phys. Rev.* **B1**, 2211 (1970).
55. H. Ikeda and K. Hirakawa, *Solid State Commun.* **14**, 529 (1974).
56. J. W. Lynn *et al.*, *Phys. Rev. Lett.* **63**, 2606 (1989).
57. R. K. Pathria, *Statistical Mechanics* (Pergamon Press, Elmsford, New York, 1972).
58. N. Metropolis and *et al.*, *J. Chem. Phys.* **21**, 1087 (1953).
59. M. E. Fisher, *Rep. Prog. Phys.* **30**, 615 (1967).
60. T. T. Wu, B. M. McCoy, C. A. Tracy and E. Barouch, *Phys. Rev.* **B13**, 316 (1976).
61. S. B. Zhang and A. Zunger, *Phys. Rev.* **B53**, 1343 (1996).
62. C. Stampfl *et al.*, *Phys. Rev. Lett.* **83**, 2993 (1999).
63. A. Li, F. Liu and M. G. Lagally, *Phys. Rev. Lett.* **85**, 1922 (2000).
64. C. Rottman and M. Wortis, *Phys. Rev.* **B24**, 6274 (1981).
65. R. K. P. Zia and J. E. Avron, *Phys. Rev.* **B25**, 2042 (1982).
66. C. Davisson and L. H. Germer, *Phys. Rev.* **30**, 705 (1927).
67. J. R. Arthur and J. J. LePore, *J. Vac. Sci. Technol.* **6**, 545 (1969).
68. A. Y. Cho, *J. Appl. Phys.* **47**, 2841 (1976).
69. A. Zangwill, *Physics at Surfaces* (University Press, Cambridge, 1988).
70. W. G. Schmidt, S. Mirbt and F. Bechstedt, *Phys. Rev.* **B62**, 8087 (2000).
71. L. J. Whitman *et al.*, *Phys. Rev. Lett.* **79**, 693 (1997).
72. S. Mirbt, N. Moll, K. Cho and J. D. Joannopoulos, *Phys. Rev.* **B60**, 13283 (1999).
73. J. Massies, P. Etienne, F. Dezaly and N. T. Linh, *Surf. Sci.* **99**, 121 (1980).

74. W. Ranke, P. Drathen and K. Jacobi, *Surf. Sci.* **77**, L162 (1978).
75. S. M. Newstead, R. A. A. Kubiak and E. H. C. Parker, *J. Cryst. Growth* **81**, 49 (1987).
76. T. Ohno, *Phys. Rev. Lett.* **70**, 631 (1993).
77. V. P. LaBella *et al.*, *J. Vac. Sci. Technol.* **A18**, 1492 (2000).
78. D. Gammon *et al.*, *Science* **273**, 87 (1996).
79. C. S. Lent and P. I. Cohen, *Surf. Sci.* **139**, 121 (1984).